Independent Component Analysis for Phase and Residual Frequency Offset Compensation in OQAM Multicarrier Systems

Jian Zhao and Paul D. Townsend

***Abstract*—Phase noise in the offset quadrature amplitude modulation (OQAM) multicarrier system results in not only constellation rotation but also crosstalk from the unique intrinsic imaginary interference (IMI). Therefore, the method for phase and residual frequency offset (RFO) compensation should be designed specifically to address this. In this paper, we exploit the statistical difference of the OQAM signal and the IMI, and propose a novel independent component analysis (ICA) based method for phase and RFO compensation. It is proved that the signal exhibits the minimal entropy with the probability distribution deviating from the Gaussian one the most when the phase is correctly compensated. Several metrics and a recursive algorithm are proposed to separate the signal and the IMI. Simulations and experiments are performed to verify the proposed theory and to compare the ICA method with modified blind phase search (M-BPS), constellation classification (CC), and Kalman filtering (KL). It is shown that the ICA method exhibits significantly better tolerance to the laser linewidth and RFO than CC and KL, and greatly reduces the complexity compared to M-BPS. Therefore, the proposed ICA method can be the most promising solution for phase and RFO compensation in OQAM multicarrier systems.**

***Index Terms*— Coherent detection, OQAM, phase noise and independent component analysis**

I. Introduction

Offset quadrature amplitude modulation (OQAM) is an interesting format for multicarrier systems because it greatly relaxes the required signal spectral profile for subcarrier orthogonality [1-7]. In the literature, this technique has been widely investigated and shows advantages in various application scenarios, including higher spectral efficiency by eliminating the guard interval in coherent detection [2], reduced crosstalk in super-channels and radio-over fiber systems [3, 4], relaxed synchronization requirement in access networks [5, 6], and improved performance in bandwidth-limited systems [7].

In OQAM multicarrier systems, the real and imaginary parts of the signal are decoded separately and intrinsic imaginary interference (IMI) exists. Consequently, the channel and phase compensation in OQAM systems are different from those in conventional QAM and should be designed specifically [8-18]. Current research has achieved channel compensation for any transmission distance without any guard interval [14]. On the other hand, studies are still required to improve the performance of phase compensation in OQAM systems. In [16], a modified blind phase search (M-BPS) method was designed for the OQAM format. This method provides superior performance for phase compensation but requires a high complexity. Constellation classification (CC) and Kalman filtering (KL) were proposed to reduce the complexity [17, 18]. However, these methods show degraded tolerance to the laser linewidth and residual frequency offset (RFO).

In this paper, we explore the statistical difference between the signal and the IMI for the first time, and propose a novel independent component analysis (ICA) based method for phase and RFO compensation. It is proved that when the phase is correctly compensated, the signal exhibits the minimal entropy with the probability distribution deviating from the Gaussian one the most. As the phase error increases, the signal mixes with the IMI and approaches a Gaussian distribution. We propose several metrics and a recursive algorithm to exploit this property and compensate the phase and RFO. Simulations and experiments are performed to verify the proposed theory and to compare the proposed ICA method with previously reported M-BPS, CC and KL. The results show that the ICA method exhibits significantly better performance than CC and KL, and greatly reduces the complexity compared to M-BPS. This makes the proposed ICA method a promising solution for phase and RFO compensation in OQAM multicarrier systems.

II. Principle

In this section, we will firstly show how the phase noise influences the OQAM system, which is significantly different from that in conventional QAM due to the IMI. Then we briefly review the M-BPS, CC and KL methods. Next, we will explore the unique feature of the OQAM system, specifically the statistical difference between the signal and the IMI, and derive the ICA-based method to compensate the phase noise and RFO. Finally, the complexities of the ICA, M-BPS, CC, and KL methods are discussed and compared.

Manuscript was received on Nov. 22, 2019. This work was supported by National Natural Science Foundation of China (61971199), Guangdong Science and Technology Plan Project (2019A050503003), Guangzhou Science and Technology Plan Project (201904010298), Fundamental Research Funds for the Central Universities, and Science Foundation Ireland (12/RC/2276_P2).

Jian Zhao is with School of Electronic and Information Engineering, the South China University of Technology, Guangzhou, China (Email: zhaojian@scut.edu.cn).

Paul Townsend is with Tyndall National Institute, Lee Maltings, Dyke Parade, Cork, Ireland. (Email: paul.townsend@tyndall.ie)

Color versions of one or more of the figures in this paper are available online at http://ieeexplore.ieee.org.

Digital Object Identifier:

This article has been accepted for publication in a future issue of this journal, but has not been fully edited. Content may change prior to final publication. Citation information: DOI 10.1109/JLT.2020.2983413, Journal of Lightwave Technology

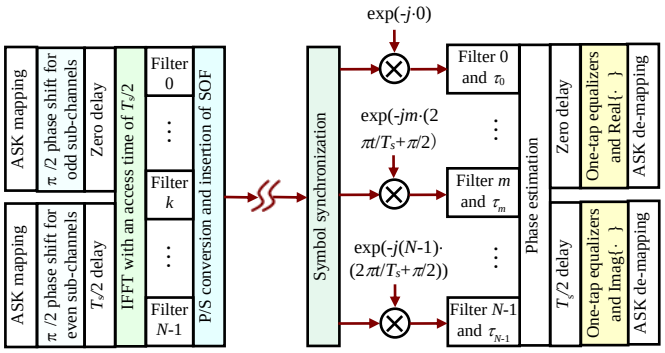

Fig. 1. Principle of the OQAM multicarrier system.

Fig. 1 shows the principle of the OQAM multicarrier system. Assuming that $a_{i,n}$ is the data of the n^{th} subcarrier in the frequency domain for the i^{th} symbol. The in-phase tributary $a_{i,n}^{real}$ and the quadrature tributary $a_{i,n}^{imag}$ are processed separately at the transmitter. For the in-phase tributary, the phase of the n^{th} subcarrier is set as $\exp(j\pi n/2)$. Conversely, for the quadrature tributary, the phase of the n^{th} subcarrier is set as $\exp(j\pi(n+1)/2)$. The quadrature tributary is then delayed by half of the symbol period (defined as $T_s/2$) or $N/2$ in the discrete domain with respect to the in-phase tributary, where N is the number of subcarriers. An inverse fast Fourier transform (IFFT) is used to generate the time-domain signals, which then pass finite impulse response (FIR) filters for pulse shaping. Assuming that $s(i\cdot N+k)$ is the k^{th} sample for the i^{th} OQAM symbol, it is derived that [2]:

$$s(i\cdot N+k)=\sum_{p=-\infty}^{+\infty}h_{filter}(i\cdot N+k-p\cdot N)\cdot s_{p,k}^{real}+\sum_{p=-\infty}^{+\infty}h_{filter}(i\cdot N+k-N/2-p\cdot N)\cdot s_{p,k}^{imag} \quad (1)$$

where $s_{p,k}^{real}$ and $s_{p,k}^{imag}$ are the IFFT of $a_{p,n}^{real}\cdot\exp(j\pi n/2)$ and $a_{p,n}^{imag}\cdot\exp(j\pi(n+1)/2)$, respectively. $h_{filter}(\cdot)$ is the impulse response of the FIR filter. In the channel, the signal experiences different effects including transceiver response, chromatic dispersion (CD) and polarization mode dispersion (PMD).

At the receiver, the m^{th} subcarrier is demodulated by multiplying the received signal with $\exp(-2\pi jkm/N-j\pi m/2)$ and passing a matched filter. The sampling point of the quadrature tributary is delayed by half of the symbol period with respect to that of the in-phase tributary. In previous works, it has been shown that in contrast to conventional QAM, the OQAM system can achieve channel compensation for any CD values without a guard interval (GI) or additional frequency-domain equalization, even when the channel memory length is much larger than the OQAM symbol period. This is because the orthogonality between the signal and the IMI is still maintained even when the dispersion induces different time delays and phases over subcarriers [14]. For example, for a 30-GBaud signal with 128 subcarriers, the symbol period is ~4.23 ns. After 1200 km of single-mode fiber (SMF), the CD-induced delay difference between subcarriers at the highest and lowest frequencies is 4.9 ns. However, if each subcarrier is sampled at the correct sampling point, i.e. at τ_m in Fig. 1 (note that there is still an additional $T_s/2$ delay for the sampling points of the quadrature tributary), the IMI is still orthogonal to the signal. In practice, τ_m can be readily obtained using a training sequence (TS). On the other hand, channel effects with a short memory length, including the transceiver response, PMD and CD-induced pulse broadening for each subcarrier, can be equalized by updating the coefficients of the matched filter without additional complexity. For example, the CD of 1200 km of SMF also results in ~38.3 ps pulse broadening on the pulse of each subcarrier, which can be compensated by updating the filters at the receiver in Fig. 1. Under the above channel compensation, the signals ($a_{i,m}^{real}$ and $a_{i,m}^{imag}$) are orthogonal to the IMI (denoted as $c_{i,m}^{real}$ and $c_{i,m}^{imag}$ respectively), and the sampled values for the two tributaries can be written as:

$$I_{i,m}^{real}=H_b(m/T_s)\cdot\exp(j\varphi_i)\cdot(a_{i,m}^{real}+j\cdot c_{i,m}^{real}) \quad (2\text{-}1)$$

$$I_{i,m}^{imag}=H_b(m/T_s)\cdot\exp(j\varphi_i)\cdot(j\cdot a_{i,m}^{imag}+c_{i,m}^{imag}) \quad (2\text{-}2)$$

where the channel effect degenerates to a constant, $H_b(m/T_s)$, for each subcarrier, and $\exp(j\varphi_i)$ is the phase noise. The desirable signals are decoded from $I_{i,m}^{real}$ and $I_{i,m}^{imag}$ as:

$$b_{i,m}^{real}=\mathrm{Re}\{H_{equ}(m/T_s)\cdot\exp(j\varphi_{i,est})\cdot I_{i,m}^{real}\} \quad (3\text{-}1)$$

$$b_{i,m}^{imag}=\mathrm{Im}\{H_{equ}(m/T_s)\cdot\exp(j\varphi_{i,est})\cdot I_{i,m}^{imag}\} \quad (3\text{-}2)$$

where $\varphi_{i,est}$ and $H_{equ}(m/T_s)$ are the compensated phase and the coefficient of the one-tap equalizer, respectively. Because $H_b(m/T_s)$ changes slowly over time, it can be estimated by the TS and compensated by $H_{equ}(m/T_s)$. In the following analysis, in order to simplify the mathematical representation, we neglect the term of $H_b(m/T_s)$ in Eq. (2) and $H_{equ}(m/T_s)$ in Eq. (3).

Note that in Eq. (2) and Eq. (3), it is assumed that the channel response and the phase noise on the in-phase and quadrature tributaries are the same. This is generally valid in practical systems. When there is a slight difference between the two tributaries, the phase/channel estimation can be performed separately for the two tributaries. It is also noted that Eqs. (2)-(3) are applicable to polarization-multiplexed systems because phase estimation is performed after polarization demultiplexing, which can be readily realized via butterfly filters.

A. Influence of the phase noise on the OQAM system

We will show how the phase noise in Eq. (2) influences the performance of the OQAM system. Fig. 2 depicts $I_{i,m}^{real}$ ((a)&(c)) and $I_{i,m}^{imag}$ ((b)&(d)) as defined in Eq. (2) for a 240-Gbit/s dual-polarization (DP) 16OQAM system, where the phase φ_i is 0 ((a)&(b)) and -π/6 ((c)&(d)). The optical signal to noise ratio (OSNR) is 25 dB. When φ_i is 0, the desirable signals of $a_{i,m}^{real}$ and $a_{i,m}^{imag}$ can be obtained by extracting the real part in Fig. 2(a) and the imaginary part in Fig. 2(b), respectively. However, when φ_i is not equal to 0, extracting the real part in Fig. 2(c) and the imaginary part in Fig. 2(d) results in the interference from the IMI. To clearly see the impact, Fig. 3 shows the decoded signal, $b_{i,m}^{real}+j\cdot b_{i,m}^{imag}$, for different φ_i when $\varphi_{i,est}$ is set to zero. It is seen that in contrast to conventional

This article has been accepted for publication in a future issue of this journal, but has not been fully edited. Content may change prior to final publication. Citation information: DOI 10.1109/JLT.2020.2983413, Journal of Lightwave Technology

QAM, the phase error disperses the constellation points in the OQAM system in addition to a phase rotation. This is because the Re{·} and Im{·} operations in Eq. (3) induce the interference from the IMI when φ_i-$\varphi_{i,est}$ is not equal to 0.

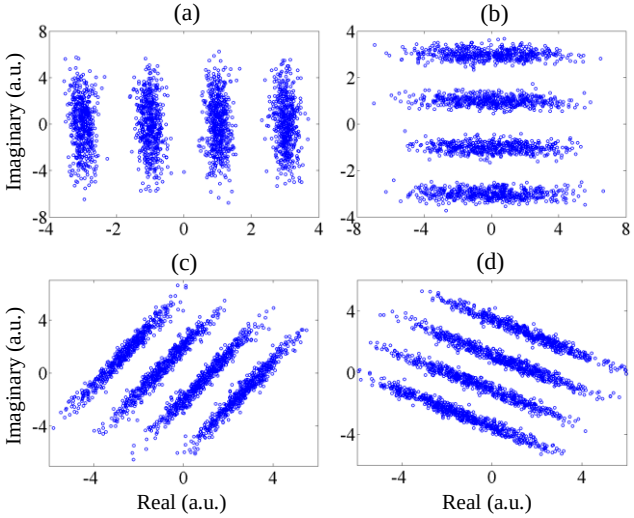

Fig. 2. $I_{i,m}^{real}$ ((a)&(c)) and $I_{i,m}^{imag}$ ((b)&(d)) in a 240-Gbit/s 16OQAM system. φ_i is 0 in (a)&(b) and -π/6 in (c)&(d). The OSNR is 25 dB.

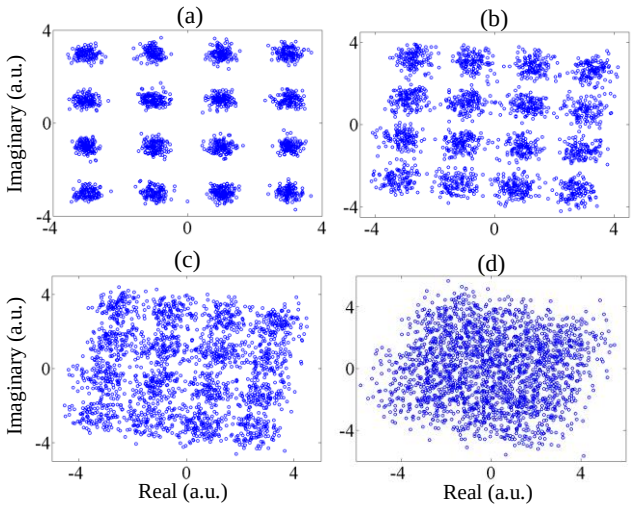

Fig. 3. The decoded 16OQAM signal when the phase φ_i is (a) 0, (b) -π/18, (c) -π/12, and (d) -π/6. The phase $\varphi_{i,est}$ is set to zero. The OSNR is 25 dB.

B. Existing compensation methods for the OQAM system

Because the phase noise in the OQAM system influences the performance differently from that in conventional QAM, phase compensation should be designed specifically. In the literature, three methods have been proposed and will be used in this paper for comparison.

The first method is called M-BPS [16]. Its principle is similar to BPS in conventional QAM and the main difference is that the signal constellation used to search the optimal phase is $b_{i,m}^{real} + j \cdot b_{i,m}^{imag}$ obtained by Eq. (3). The optimal $\varphi_{i,est}$ in the equation is the one that can achieve the minimal Euclidean distance to the desired constellation. This method achieves superior performance provided that the number of tested phases is sufficient. However, it requires a high complexity and is generally used as the benchmark for performance comparison.

The second method is called CC [17]. Taking 16OQAM in Fig. 2(d) as an example, this method firstly makes pre-decisions to classify the samples in the constellation to four signal levels. Then a linear function is implemented to fit the samples for each signal level, and the estimated phase is $\tan^{-1}$(the slope of the linear fitting function). This method reduces the complexity. However, it is sensitive to the pre-decision errors and exhibits reduced tolerance to the laser linewidth and RFO.

The last one is called KL [18]. Its principle is similar to the KL method in conventional QAM but the wise decision (WD) should be adapted to the OQAM signal. It has been shown in [18] that this method exhibits better performance under small laser linewidths due to its capability to compensate both phase and amplitude noise. However, as shown in [18] and will be shown later, this method exhibits poor tolerance to the laser linewidth and RFO due to the WD errors.

C. The proposed ICA-based method

In this subsection, we will exploit the statistical property of the signal and the IMI to compensate the phase. From Fig. 2, it is shown that the constellations of $I_{i,m}^{real}$ and $I_{i,m}^{imag}$ are similar except for a $\pi/2$ phase rotation. Therefore, without the loss of generality, we discuss the phase estimation as follows only based on $I_{i,m}^{real}$. From Eq. (2), it is derived that

$$\begin{bmatrix} \mathrm{Re}\{I_{i,m}^{real}\} \\ \mathrm{Im}\{I_{i,m}^{real}\} \end{bmatrix} = \begin{bmatrix} \cos(\varphi_i) & -\sin(\varphi_i) \\ \sin(\varphi_i) & \cos(\varphi_i) \end{bmatrix} \times \begin{bmatrix} a_{i,m}^{real} \\ c_{i,m}^{real} \end{bmatrix} \quad (4)$$

Note that we have neglected the term $H_b(m/T_s)$ in Eq. (2) because it can be well compensated by $H_{equ}(m/T_s)$. Firstly, we would like to indicate that the variances of $a_{i,m}^{real}$ and $c_{i,m}^{real}$ are similar. This can be readily proved by numerically calculating the variances of the signal and the IMI in Fig. 2. In fact, if their variances are different, φ_i in Eq. (4) can be estimated by a simpler method called principal component analysis (PCA). However, if their variances are the same, PCA cannot recover $a_{i,m}^{real}$ and $c_{i,m}^{real}$ from the received $I_{i,m}^{real}$ and ICA that can separate independent signals from their combinations [19-21] is proposed to solve the problem. In the following, we assume the variances of $a_{i,m}^{real}$ and $c_{i,m}^{real}$ are σ^2. Fig. 4 shows the probability density function (PDF) of the real and imaginary parts of $I_{i,m}^{real}$. The PDF is calculated using 54000 samples. It is seen that when φ_i is 0, that is $\mathrm{Re}\{I_{i,m}^{real}\} = a_{i,m}^{real}$ and $\mathrm{Im}\{I_{i,m}^{real}\} = c_{i,m}^{real}$, their statistical difference is the most significant. Specifically, the PDF of $a_{i,m}^{real}$ concentrates on four points, deviating from the Gaussian distribution the most, while that of $c_{i,m}^{real}$ is close to a Gaussian one. In theory, the IMI is the combination of the crosstalk from multiple symbols of adjacent subcarriers as well as the other quadrature of the same subcarrier. From the central limit theorem, the IMI approaches a Gaussian distribution. On the other hand, as φ_i deviates from zero, $\mathrm{Re}\{I_{i,m}^{real}\}$ approaches a Gaussian distribution as well and the statistical difference between the real and imaginary parts reduces.

This article has been accepted for publication in a future issue of this journal, but has not been fully edited. Content may change prior to final publication. Citation information: DOI 10.1109/JLT.2020.2983413, Journal of Lightwave Technology

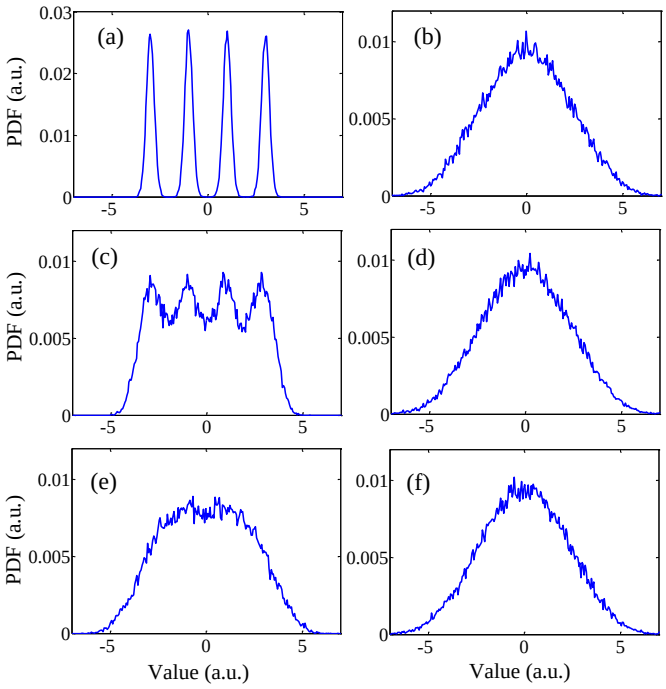

Fig. 4. The PDF of the real ((a), (c), (e)) and imaginary ((b), (d), (f)) parts of $I_{i,m}^{real}$ in a 240-Gbit/s 16OQAM system. φ_i is (a)&(b) 0, (c)&(d) -π/12 and (e)&(f) -π/6. The PDF is calculated using 54000 samples. The OSNR is 25 dB.

In Appendix I, we analyze the above phenomenon from the information theory and prove that when the PDF of

$$b_{i,m}^{real} = \left[\cos(\varphi_{i,est}) \quad -\sin(\varphi_{i,est})\right] \begin{bmatrix} \mathrm{Re}\{I_{i,m}^{real}\} \\ \mathrm{Im}\{I_{i,m}^{real}\} \end{bmatrix} \tag{5}$$

deviates from the Gaussian one the most or the entropy $H(b_{i,m}^{real})$ is minimized, the $\varphi_{i,est}$ is the desired phase and $b_{i,m}^{real} = a_{i,m}^{real}$.

In theory, a metric to evaluate how far a distribution is from the Gaussian distribution is the kurtosis [19]:

$$Kur = \mu_4 / \sigma^4 - 3 \tag{6}$$

where μ_4 is the four-order moment. *Kur* is zero for the Gaussian distribution, and is the most negative for the distribution when there is no phase error, as shown in Fig. 4(a).

Because σ is a constant regardless of $\varphi_{i,est}$, we can minimize μ_4 of $b_{i,m}^{real}$ to obtain the desirable phase $\varphi_{i,est}$ in Eq. (5). However, this metric does not give a high sensitivity to the change of the PDF profile and consequently the phase error φ_i-$\varphi_{i,est}$. In this paper, we propose a general metric μ_x to estimate the phase, where x is an even number no less than 4. Fig. 5(a) shows μ_x versus φ_i-$\varphi_{i,est}$ for different x values. μ_x is obtained by calculating the high-order moments of $b_{i,m}^{real}$. It is seen that the value of μ_x is minimal at $\varphi_{i,est}=\varphi_i$ for all x values. The curve with a larger x value is steeper at φ_i-$\varphi_{i,est}$=0, implying that it is easier to identify the point of φ_i-$\varphi_{i,est}$=0 using a larger x.

Although the value of μ_x is minimal at $\varphi_{i,est}=\varphi_i$ in theory, a finite number of samples has to be used in practice to estimate μ_x. In this case, the minimal point does not always occur at $\varphi_{i,est}=\varphi_i$, resulting in estimation errors. Fig. 5(b) shows the variance of the estimation error versus the number of samples for different x values. In the figure, we use 200 sets of samples with the number of samples in each set varying from 20 to 500. In each set, we calculate the μ_x versus φ_i-$\varphi_{i,est}$ curve similar to Fig. 5(a) and find the φ_i-$\varphi_{i,est}$ that gives the minimal μ_x. Then we calculate the variance of φ_i-$\varphi_{i,est}$ based on the 200 sets of samples. It is clear from Fig. 5(b) that x=4 results in a large variance. The use of x=6 significantly reduces the variance. The curves for x=8 and x=10 are similar. Note that the variance may not fully reflect the bit error rate (BER) performance. As described later, x=6 is sufficient for 16OQAM to achieve the saturated BER performance. A larger x may bring performance benefit for higher format levels, which are more sensitive to the phase noise. However, an algorithm should be used in practice to recursively search the minimal point of μ_x. It is found that a larger x value may induce instability during the convergence of the algorithm for large linewidths and RFOs. Therefore, the optimal x should be the minimal one that achieves the saturated performance. Note that a larger x does not increase the complexity as will be discussed later.

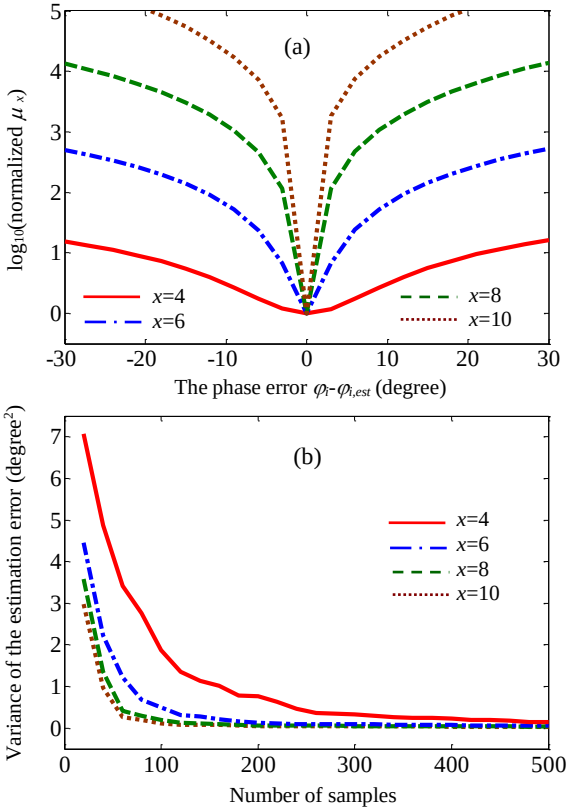

Fig. 5. (a) $\log_{10}(\mu_x)$ versus φ_i-$\varphi_{i,est}$ for different x values. μ_x is normalized such that the minimal value is zero for all x; (b) Variance of the estimation error versus the number of samples for different x values.

A recursive algorithm is proposed to obtain the desirable $\varphi_{i,est}$ by adaptively searching the minimal μ_x. Assume that $\mathbf{r}_i=[r_{i,1}, r_{i,2}\ldots r_{i,P}]$ are the samples used to estimate the phase $\varphi_{i,est}$. In practice, $\mathbf{r}_i$ include the samples of both $I_{k,m}^{real}$ and $-j\cdot I_{k,m}^{imag}$, where k=…i-1, i, i+1… and m=1…N. That is, $\mathbf{r}_i$ consist of the samples of all subcarriers and the symbols around the i^{th} symbol. For example, when the subcarriers of the (i-1)-th, the i-th, and the (i+1)-th symbols are used to estimate $\varphi_{i,est}$, P=6N. Note that

in contrast to conventional QAM, the available number of samples for phase estimation is doubled in OQAM systems because both $I_{k,m}^{real}$ and $-j\cdot I_{k,m}^{imag}$ can be used. It is also noted that although $\mathrm{Re}\{\mathbf{r}_i\}$ and $\mathrm{Im}\{\mathbf{r}_i\}$ have the same variance σ^2 in principle, normalization of $\mathrm{Re}\{\mathbf{r}_i\}$ and $\mathrm{Im}\{\mathbf{r}_i\}$ can eliminate statistical discrepancy when P is small. This normalization however may not be necessary for a large P (>100). The phase is obtained recursively by:

$$\mathbf{b}_i = \mathbf{W}_i \times \begin{bmatrix} \mathrm{Re}\{\mathbf{r}_i\} \\ \mathrm{Im}\{\mathbf{r}_i\} \end{bmatrix} \tag{7-1}$$

$$\begin{aligned} \mathbf{W}_{i,new} &= \mathbf{W}_{i,old} - \alpha \cdot E\{\frac{\partial \mathbf{b}_i^x}{\partial \mathbf{W}_i}\} \\ &= \mathbf{W}_{i,old} - \frac{\alpha}{P} \cdot \sum_{k=1}^{P} b_{i,k}^{x-1} \times [\mathrm{Re}\{r_{i,k}\} \;\; \mathrm{Im}\{r_{i,k}\}] \end{aligned} \tag{7-2}$$

$$\mathbf{W}_{i,new} = \mathbf{W}_{i,new} / \left\| \mathbf{W}_{i,new} \right\| \tag{7-3}$$

where $\mathbf{W}_i=[\cos(\varphi_{i,est}) \;\; -\sin(\varphi_{i,est})]$ is the compensation vector; $\mathbf{b}_i^x$ is the x-th power of $\mathbf{b}_i$; α is a step size to be optimized; $\|\cdot\|$ is the norm of the vector. Eq. (7-2) describes the recursive process. As will be shown later, 2~3 iterations are sufficient to achieve the optimal performance. In Eq. (7-2), the $(x\text{-}1)$-th power of $\mathbf{b}_i$ should be calculated for the estimation. This can be realized by employing a look-up table as described later so that the complexity of this step is independent of the value of x.

D. Complexity of different phase compensation methods

In this subsection, we will compare the complexity of the proposed ICA method with that of M-BPS, CC and KL. In contrast to conventional QAM, the phase ambiguity in the OQAM system is π instead of $\pi/2$. This problem can be solved by comparing the estimated phases between adjacent symbols. The complexity here excludes the correction of phase ambiguity because it is applied to all methods and does not influence the comparison. It is also noted that the calculated complexity is based on a multicarrier symbol consisting of all subcarriers in that symbol. Finally, without the loss of generality, we use 16OQAM in the analysis.

In the ICA method, Eq. (7-1) requires $2P$ real multiplications and P real adders. $b_{i,k}^{x-1}$ in Eq. (7-2) can be obtained as follows: because the variance of $b_{i,k}$ is σ^2, we quantize $b_{i,k}$ in the range of $[-2\sigma \; 2\sigma]$ and build up a look-up table that maps the quantized $b_{i,k}$ to $b_{i,k}^{x-1}$. It will be shown later that a 3-bit resolution is sufficient to obtain the optimal performance. The complexity of the quantization is $P\cdot Q_{\mathrm{ICA}}$ comparisons, where Q_{ICA} is the bit resolution. Based on this, the total complexity of Eq. (7-2) is $P\cdot Q_{\mathrm{ICA}}$ comparisons, $2P$+2 real multiplications and $2P$ real additions. Finally, the normalization in Eq. (7-3) requires 5 real multiplications and 1 real addition. Eq. (7) is iterated for convergence. The total complexity is $U(4P+7)$ real multiplications, $U(3P+1)$ real additions and UPQ_{ICA} comparisons, where U is the number of iterations.

In M-BPS [16], we firstly calculate the complexity for each tested phase, $\exp(-j\pi p/B)$, where B is the number of tested phases and p=0…B-1. The samples firstly multiply the phase to obtain $\mathrm{Re}\{ I_{k,m}^{real} \cdot\exp(-j\pi p/B)\}+j\cdot\mathrm{Im}\{ I_{k,m}^{imag} \cdot\exp(-j\pi p/B)\}$. Note that $I_{k,m}^{real}$ and $I_{k,m}^{imag}$ are combined in M-BPS and so the number of averaging is $P/2$ instead of P. The above step requires $P/2\times(2+2) = 2P$ real multiplications and $P/2\times(1+1) = P$ real additions. The obtained signals are then compared with 16QAM constellation to make pre-decisions. This step requires $P/2\times2\times\log_2(4)=2P$ comparisons. The distances between $P/2$ complex samples and their decisions are then calculated and summed. This requires $P/2\times2=P$ real multiplications and $P/2\times4\text{-}1=2P\text{-}1$ real additions. The above process is repeated for B tested phases, resulting in B times of complexity. Finally, B-1 comparisons are needed to find the optimal phase. Therefore, the total complexity is $3PB$ real multiplications, $3PB\text{-}B$ real additions and $(2P+1)B$-1 comparisons.

In the CC method, we calculate the complexity based on the principle in [17]. Pre-decision is firstly made for constellation classification. For the number of samples P, the complexity of the pre-decision (Eq. (10) in [17]) is $(P+1)$ real multiplications, $2P$ real additions and $2P$ comparators. The pre-decided symbols are then used for linear curve fitting (Eq. (8) in [17]) and the complexity of this step is $(3+2P+7)$ real multiplications and $(5P\text{-}2)$ real additions. Finally, a look-up table is used to calculate the $\tan^{-1}(\cdot)$ of the slope (Eq. (9) in [17]) and the signal quantization requires Q_{cc} comparisons, where Q_{cc} is the bit resolution. Therefore, the total complexity is $(3P+11)$ real multiplications, $(7P\text{-}2)$ real additions and $2P+Q_{\mathrm{cc}}$ comparators. Note that this complexity is different from that in [17] because that work is based on OQAM superchannels and uses a sliding window to estimate the phase of each symbol in each subcarrier separately while this work is based on electronic multi-carriers and estimates the phase of all subcarriers simultaneously.

Finally, we calculate the complexity of the KL method by following the algorithm in Table 1 of [18], with the block diagram depicted in Fig. 1(b) of [18]. Assuming that 1 complex multiplication requires 4 real multiplications and 2 real additions, the complexity for the WD decisions and two phase rotations before and after the WD decisions in Fig. 1(b) of [18] is $8P$ real multiplications, $4P$ real additions and $2P$ comparators. The complexity of the Kalman gain is $12P$ real multiplications and $7P$ real additions. The complexity to update the phase is $8P$ real multiplications and $8P$ real additions. Finally, by re-using the results in the last step, updating the correlation matrix requires 4 real multiplications and 3 real additions. Therefore, the total complexity is $28P+4$ real multiplications, $19P+3$ real additions and $2P$ comparators.

Table 1. Complexity of different compensation methods

	Multiplications	Additions	Comparators
Proposed ICA	$U(4P+7)$	$U(3P+1)$	UPQ_{ICA}
M-BPS	$3PB$	$3PB\text{-}B$	$(2P+1)B$-1
CC	$3P+11$	$7P\text{-}2$	$2P+Q_{\mathrm{cc}}$
KL	$28P+4$	$19P+3$	$2P$

Table 1 summarizes the complexity of different methods. In the table, U is the number of iterations in the ICA method. As will be shown later, U of 2 or 3 is sufficient to achieve the

optimal performance. In this paper, U=3 is used in all simulations and experiments. Q_{ICA} is the bit resolution of the look-up table. It is found that Q_{ICA}=3 can give the saturated performance. B is the number of test phases in M-BPS and is set as 32 to obtain similar performance as the ICA method. Finally, Q_{CC} is the bit resolution of the look-up table in the CC method. Fig. 6 shows the required number of multiplications versus P for different methods. U=3 and B=32. It is observed that the CC method exhibits the least complexity. However, as will be shown, the performance of this method is poorer than that of the ICA and M-BPS methods. The proposed ICA method has less complexity than the KL and M-BPS methods. It also exhibits a better tolerance to the laser linewidth and RFO than the KL method. Finally, the complexity of M-BPS is highest.

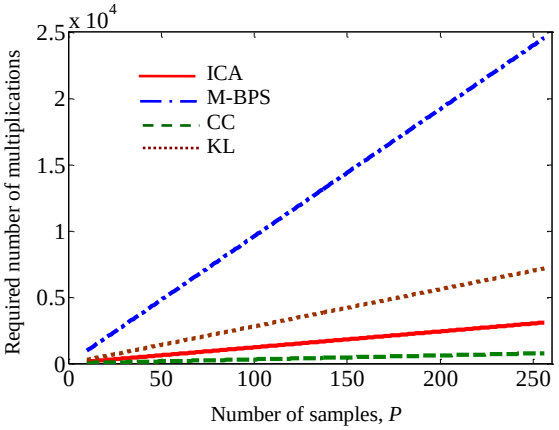

Fig. 6. Required number of multiplications versus P for different methods.

III. Simulation Setup and Results

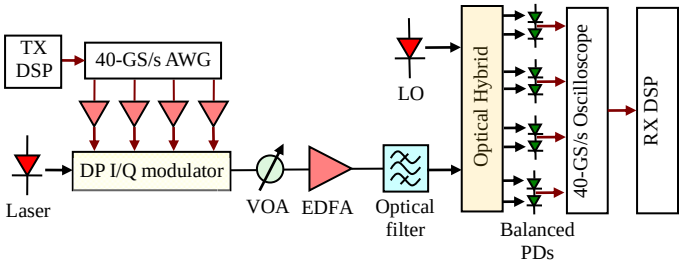

Fig. 7. Simulation model

We firstly simulated a coherent 16OQAM multi-carrier system to verify the proposed theory. Four methods were compared: M-BPS, CC, KL and the proposed ICA method. All methods were based on the same simulation parameters.

Fig. 7 depicts the simulation setup. The FFT size was 128 or 64, in which 3/4 subcarriers were modulated with data. The signal format was 16OQAM and the pulse shaping filter created a square-root-raised-cosine (SRRC) spectral profile with a roll-off factor of 0.5. The memory length of the FIR filters for pulse shaping was 4, which was sufficient to achieve optimal performance for the targeted spectral profile [2]. A training sequence (TS) was added before the payload for channel estimation. The sampling rate of the arbitrary waveform generator (AWG) was 40 GS/s. The sinc roll-off of the DACs was compensated in the digital domain. The response of the AWG was assumed to be a 5rd-order Gaussian filter with the 3-dB bandwidth equal to half of the sampling rate. The electronic signals were then amplified and modulated a CW light using a dual-polarization (DP) I/Q modulator. The total line rate was 240 Gbit/s. The laser linewidth varied for investigation. We did not add optical fibers in the simulation and focused on the phase noise. The effect of fiber transmission does not influence the conclusions and will be characterized in the experiment. At the receiver, a variable optical attenuator (VOA) was used to adjust the OSNR. The optical signal was amplified by an Erbium-doped fiber amplifier (EDFA), filtered by an optical filter with 40-GHz bandwidth, and detected by a coherent receiver. The bandwidth of the balanced photodiode (PD) was 40 GHz. The electrical signals were sampled by a 40-GS/s real-time scope. The decoding of the signal was the same as described in Section II, where the channel was estimated using the TS. The number of simulated bits was 1.28 million and the BER was obtained via direct error counting.

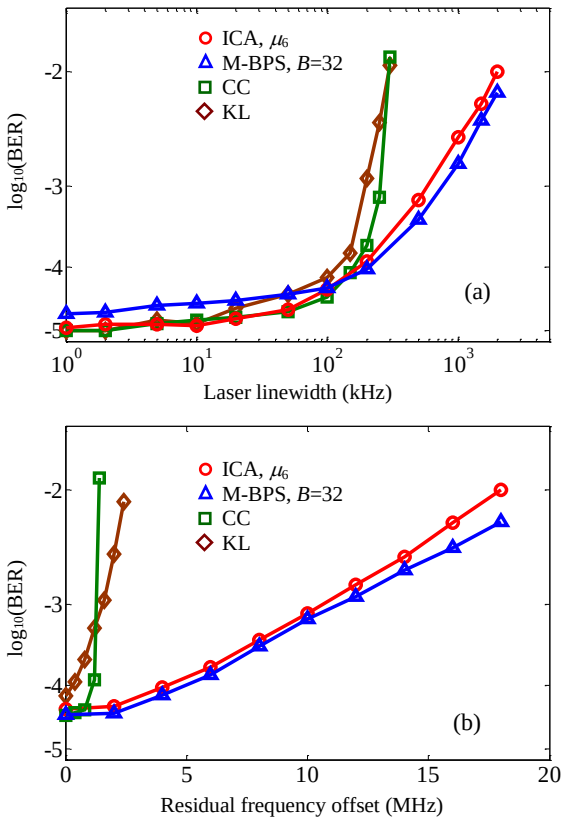

Fig. 8. BER versus (a) laser linewidth and (b) RFO between the transmitter laser and the LO at 100-kHz linewidth. The FFT size is 128.

Fig. 8(a) shows the BER versus the laser linewidth for different methods, where the linewidth is used for both the transmitter laser and the LO. The FFT size is 128 and the OSNR is 22 dB. The number of samples for estimation, P, is optimized for all methods. In ICA, the number of iterations and x in Eq. (7) are 3 and 6, respectively. The parameter α is optimized. In M-BPS, the number of tested phases, B, is 32. In KL, the measurement parameters are optimized. It is seen from Fig. 8(a) that M-BPS exhibits the best tolerance to the laser linewidth. The proposed ICA method shows slightly degraded performance compared to M-BPS. In contrast, the KL and CC methods are less tolerant to the laser linewidth. This can be attributed to the pre-decision in CC and the WD in KL. For larger linewidths, pre-decision or WD may cause errors which are fed back to the phase estimation of the next symbol and

result in performance instability. It is found that when the laser linewidth is larger than 200 kHz, the errors accumulate and the performance of these two methods is degraded significantly. In addition, the performance of the CC method is also unstable when φ_i is close to 0 or π. CC estimates the slope of the linear fitting curves (see Fig. 2) and uses $\tan^{-1}(\cdot)$ to obtain the phase. However, this slope would become infinite when φ_i is close to 0 or π (CC needs to rotate the phase by π/2 and tan(0+π/2) is infinite), around which the estimation is far from accurate. Therefore, the CC method is sensitive to not only the phase noise but also the absolute value of the phase. Fig. 8(b) shows the BER versus the RFO at 100-kHz linewidth. Similar to Fig. 8(a), M-BPS exhibits the best performance. The ICA method significantly reduces the complexity at the expense of slightly degraded performance. It is also seen that although the CC method shows better performance than the KL method in Fig. 7(a), it exhibits a poorer tolerance to the RFO. This is because the absolute phase is linearly proportional to the RFO, which easily moves the CC method into the unstable operation region.

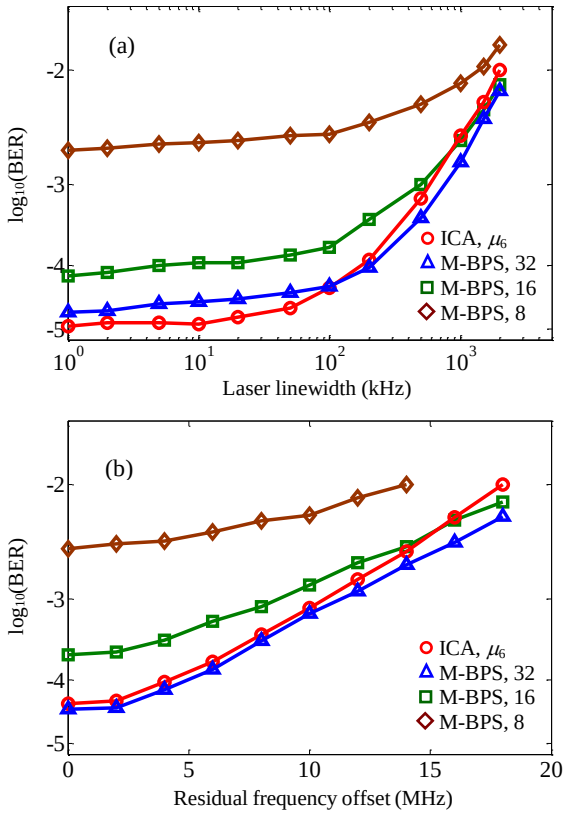

Fig. 9. Performance versus (a) laser linewidth (b) RFO between the transmitter laser and the LO at 100-kHz linewidth. The FFT size is 128.

Fig. 9 shows the performance versus (a) the laser linewidth and (b) the RFO for the ICA method and M-BPS with different numbers of tested phases. The OSNR is 22 dB. The number of samples for phase estimation is optimized for both methods. In ICA, the number of iterations and x in Eq. (7) are 3 and 6, respectively. The parameter α is optimized. It is seen that decreasing B in M-BPS reduces the estimation accuracy and consequently degrades the performance. When compared to the ICA method, M-BPS with B of 16 shows moderate penalties for small linewidths and RFOs while significant penalties are observed for M-BPS with B of 8. Therefore, M-BPS with B of 32 is used in this paper. Note that a large B results in higher complexity and the ICA method exhibits much less complexity than M-BPS with B of 32, as shown in Fig. 6.

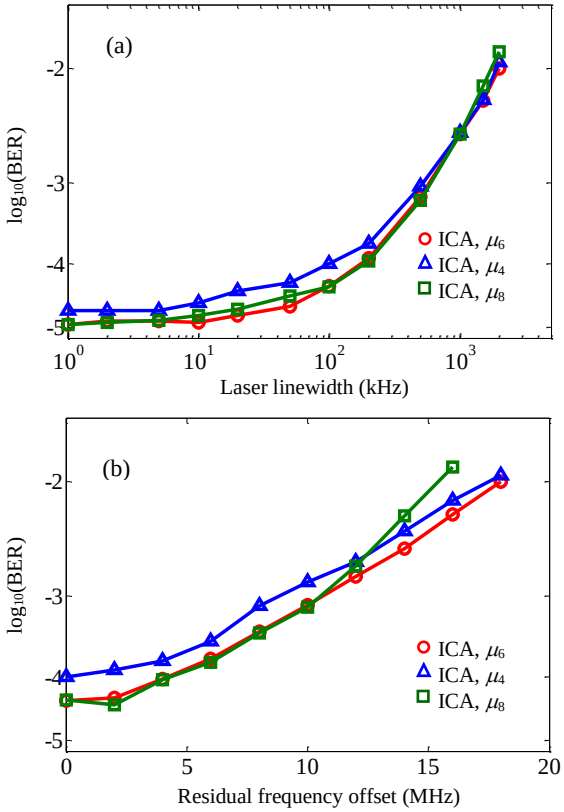

Fig. 10. Performance versus (a) laser linewidth and (b) RFO between the transmitter laser and the LO at 100-kHz linewidth. The FFT size is 128.

As shown in Fig. 5, a larger number of x in the ICA method results in reduced estimation errors. Fig. 10 depicts the BER performance versus the laser linewidth and the RFO for the ICA method with different x values. The number of iterations is 3 and the parameter α in Eq. (7-2) is optimized. It is seen that μ_6 indeed gives a better performance than μ_4 due to a smaller variance of estimation error, as shown in Fig. 5(b). However, the BER performance is no longer improved by further increasing x. Note that the results in Fig. 5(b) do not consider the algorithm of Eq. (7) to recursively search the minimal point. Although μ_8 can provide a smaller variance of estimation error, it may result in the instability of convergence for large linewidths and RFOs, as shown in Fig. 10. Consequently, μ_6 is an optimal metric to balance the accuracy and the convergence. Note that this conclusion is based on 16OQAM. For higher format levels such as 64OQAM, μ_8 or higher-order moments may bring benefits because these formats are more sensitive to the phase noise and require smaller variances of estimation error to eliminate performance penalty.

The complexity of the proposed ICA method depends on the number of iterations in the algorithm and the resolution of the look-up table, as shown in Table 1. Fig. 11 shows the performance versus the number of iterations for μ_6. It is seen that when the impairment is moderate (circles), 1 iteration is sufficient. Even when the impairments are severe (triangles and

squares), 2~3 iterations can still achieve the optimal performance. Fig. 12 depicts the performance versus the resolution of the look-up table to calculate $b_{i,k}^{x-1}$. It is shown that 3 bits are sufficient to achieve the optimal performance. These results confirm that the ICA method can indeed achieve the desirable performance with low implementation complexity.

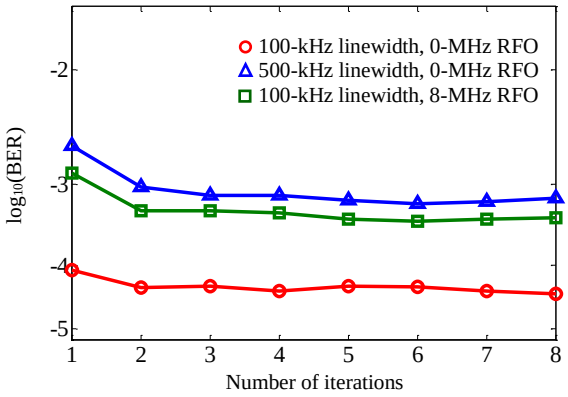

Fig. 11. Performance versus the number of iterations in the ICA method.

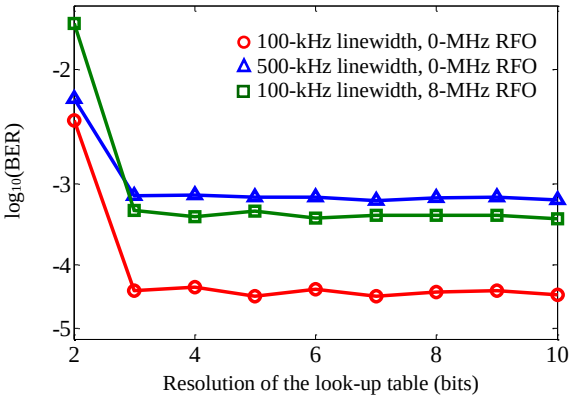

Fig. 12. $\log_{10}$(BER) versus the resolution in the ICA method.

We further investigate the cases using the FFT size of 64. Under a fixed sampling rate, a smaller number of the FFT size results in a short symbol period and consequently improved tolerance to the laser linewidth and the RFO. Fig. 13 shows the BER performance of different compensation methods. The OSNR is 22 dB. The number of samples for estimation is optimized for all methods. In ICA, the number of iteration and x in Eq. (7) are 3 and 6, respectively. In M-BPS, the number of tested phases, B, is 32. In KL, the measurement parameters are optimized. Fig. 13 implies that similar conclusions can be drawn for the FFT size of 64. The proposed ICA method exhibits significantly better performance than the CC and KL methods, and greatly reduces the complexity at the expense of slightly degraded performance compared to M-BPS. It is also seen that in contrast to Fig. 8(b), the CC method shows much poorer RFO tolerance than KL in Fig. 13(b). As described in Fig. 8, the performance of the CC method also depends on the absolute phase values, specifically the phases when the slope of the linear fitting curve become infinite. Because the absolute phase rotation is linearly proportional to the RFO, the tolerance of the CC method to the RFO does not increases as the FFT size decreases. This is in contrast to the KL method, in which the tolerance is nearly doubled by using the FFT size of 64.

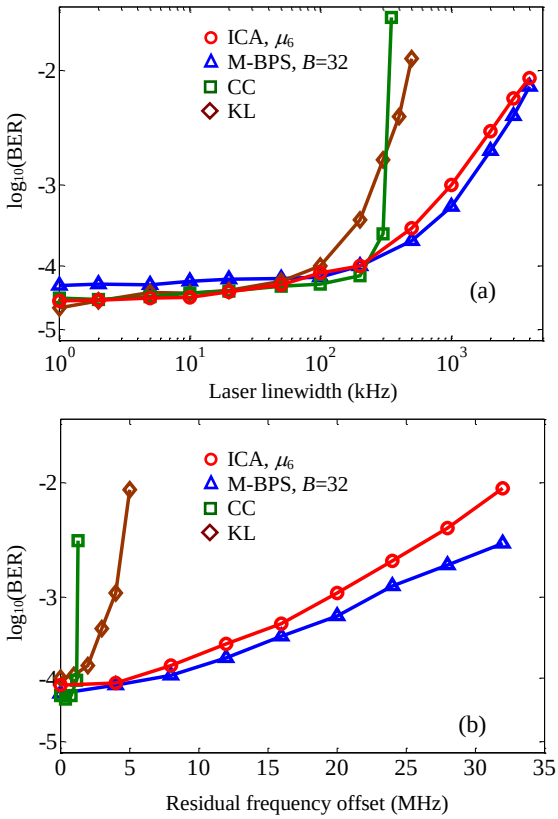

Fig. 13. BER versus (a) laser linewidth and (b) RFO between the transmitter laser and the LO at 100-kHz linewidth. The FFT size is 64.

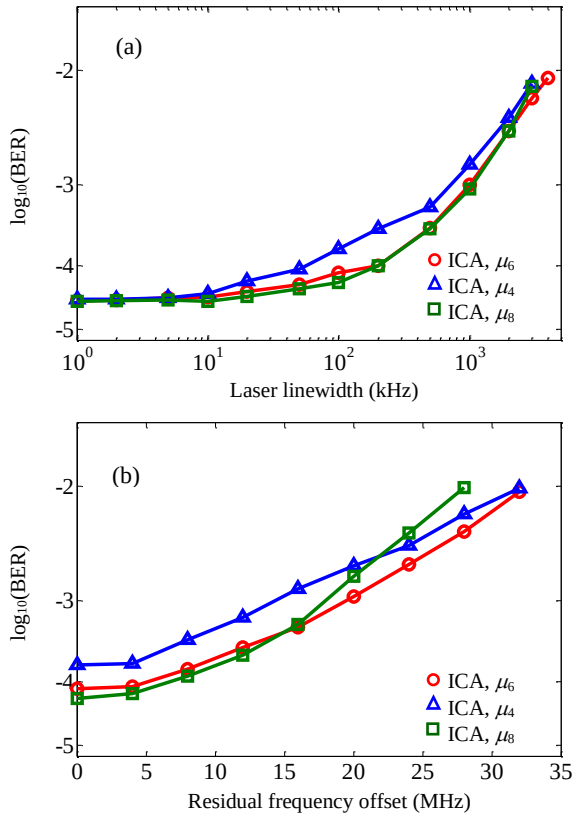

Fig. 14. Performance versus (a) laser linewidth and (b) RFO between the transmitter laser and the LO at 100-kHz linewidth. The FFT size is 64.

Fig. 14 shows the performance versus the laser linewidth and the RFO for the ICA method with different x values when the FFT size is 64. The number of iterations is 3 and the parameter α in Eq. (7-2) is optimized. We can obtain the same conclusions as those in Fig. 10. μ_4 results in a large estimation error while the performance becomes unstable for large RFOs by using μ_8. μ_6 achieves the best performance for 16OQAM by balancing the accuracy and the convergence.

IV. Experimental Setup and Results

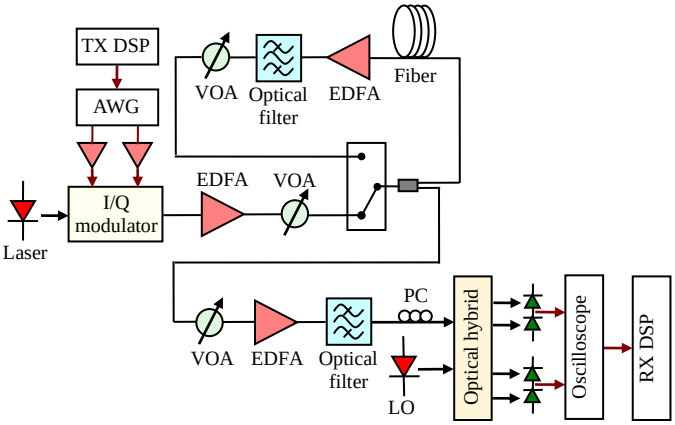

Fig. 15. Experimental setup

Experiments were then performed to verify the proposed ICA method. Fig. 15 shows the experimental setup. The FFT size was 128, of which 102 subcarriers were modulated with 16QAM data. The FIR filter created a SRRC signal pulse with a roll-off factor of 0.5. The OQAM multicarrier sequence began with a start-of-frame symbol for symbol synchronization and a TS was used for channel estimation. The generated signal was downloaded to an AWG with a 12-GS/s sampling rate. The signal baud rate was 12×102/128=9.6 GBaud.

The laser linewidth was <100 kHz. The electronic signal was fed into an I/Q modulator with the peak-to-peak driving swing of $0.5V_\pi$. The optical signal was amplified by an EDFA and sent into a recirculating loop. The fiber length in the loop was 60 km with a loss of ~14 dB. An EDFA was used in the loop to compensate the fiber loss and a 0.8-nm optical filter was employed to suppress the optical noise. At the receiver, the optical signal was pre-amplified, filtered by an optical filter with a 3-dB bandwidth of 0.64 nm, and detected by a 40-GHz coherent receiver. The powers of the optical signal and the LO were ~0 dBm and ~10 dBm, respectively. A variable optical attenuator was added before the pre-amplifier to control the OSNR. The detected signals were captured using a 50-GS/s real-time oscilloscope. The total number of measured 16QAM symbols was ~300,000.

Because the lasers in the experiment had fixed linewidth, we could not measure the tolerance to the laser linewidth. However, the RFO can be adjusted at the receiver via DSP. Fig. 16 shows the BER performance versus the RFO at back-to-back for different methods. It is confirmed that the proposed ICA method exhibits only slightly degraded performance compared to the M-BPS method. Note that the ICA method requires much lower complexity than M-BPS. On the other hand, the CC and KL methods show much poorer tolerance to the RFO compared to the ICA and M-BPS methods.

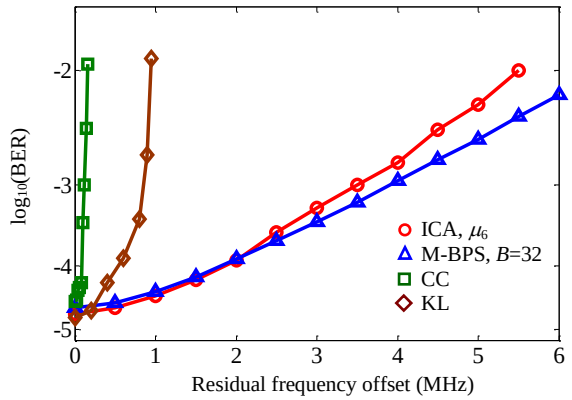

Fig. 16. Performance versus RFO at 16-dB OSNR and 0 km for different methods. In ICA, the number of iterations and x are 3 and 6, respectively. The parameter α is optimized. In M-BPS, the number of tested phases, B, is 32. In KL, the measurement parameters are optimized.

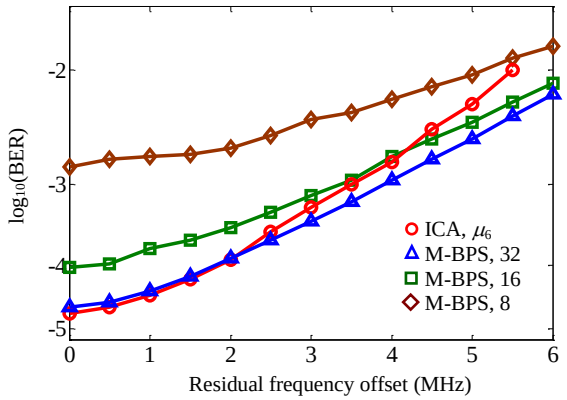

Fig. 17. Performance versus RFO at 16-dB OSNR and 0 km.

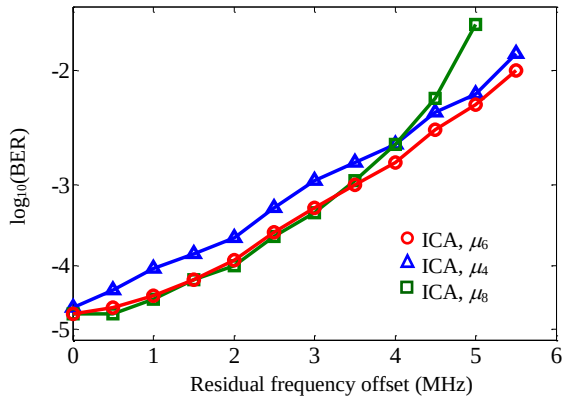

Fig. 18. Performance versus RFO for different x in the ICA method.

In Fig. 16, B is set as 32 in the M-BPS method. In order to investigate the influence of the number of tested phases, Fig. 17 depicts the BER performance versus the RFO for the ICA method and M-BPS with different B. In ICA, the number of iterations and x are 3 and 6, respectively. The parameter α is optimized. It is seen that the performance degrades as B reduces. When compared to the ICA method, M-BPS with B of 16 shows a moderate penalty for RFO values less than 4 MHz. When B is reduced to 8, significant performance degradation is observed. B of 32 avoids the penalty for small RFOs while

exhibiting better tolerance for large RFOs. However, its complexity is much higher than that of the ICA method.

Fig. 18 shows the BER performance versus the RFO for the proposed ICA method with different x values. The number of iterations is 3 and the parameter α in Eq. (7-2) is optimized. Similar to the simulation result, μ_4 shows a poorer performance than μ_6 because it results in a larger variance of estimation error as shown in Fig. 5(b). On the other hand, μ_8 can achieve a similar performance as μ_6 for small RFO values, but it is not stable for large RFO values. Consequently, as the RFO increases, the performance is degraded more rapidly. μ_6 can achieve a balance between the accuracy and the convergence, and thus exhibits the best tolerance to the RFO.

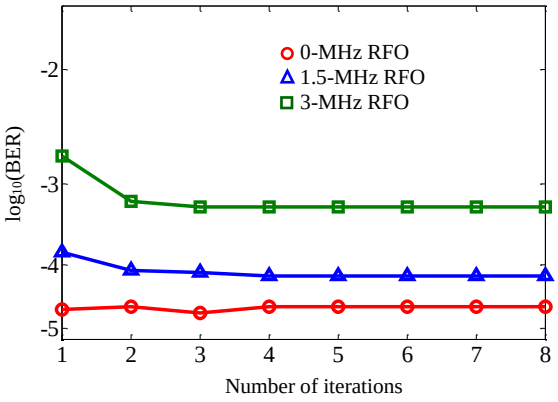

Fig. 19. Performance versus the number of iterations in the ICA method.

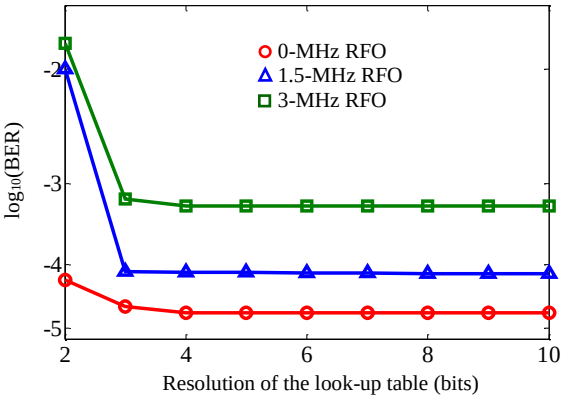

Fig. 20. Performance versus the resolution in the ICA method.

Fig. 19 shows the performance versus the number of iterations in the ICA method. It is seen that the optimal performance can be obtained by using 1~3 iterations depending on the amount of impairments. Fig. 20 depicts the performance versus the resolution of the look-up table to calculate $b_{i,k}^{x-1}$. It is confirmed that 3 bits are sufficient to achieve the optimal performance under all investigated RFO values. This confirms that the ICA method is able to achieve lower complexity than M-BPS at the expense of slightly degraded performance.

All results above are based on the back-to-back case at 16-dB OSNR. In order to further verify the theory, we compare the performance of different methods for a different OSNR value as shown in Fig. 21, and for different transmission distances as depicted in Fig. 22. It is seen that in all cases, the proposed ICA method exhibits significantly better performance than the CC and KL methods, and only slightly degraded tolerance to the RFO compared to the M-BPS method. Therefore, the advantages of this method are valid in difference scenarios regardless of the OSNR values and distances. This makes the proposed method a promising solution for phase and RFO compensation in OQAM multicarrier systems.

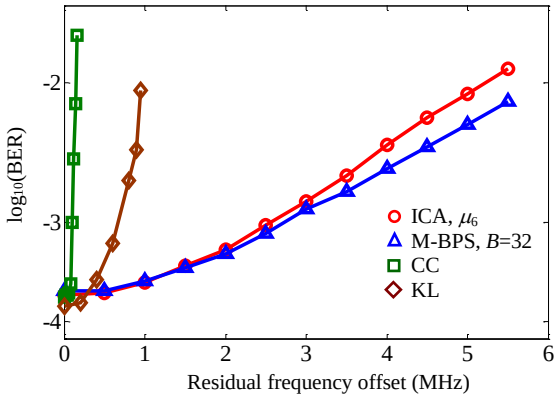

Fig. 21. Performance versus RFO at 14-dB OSNR and 0 km.

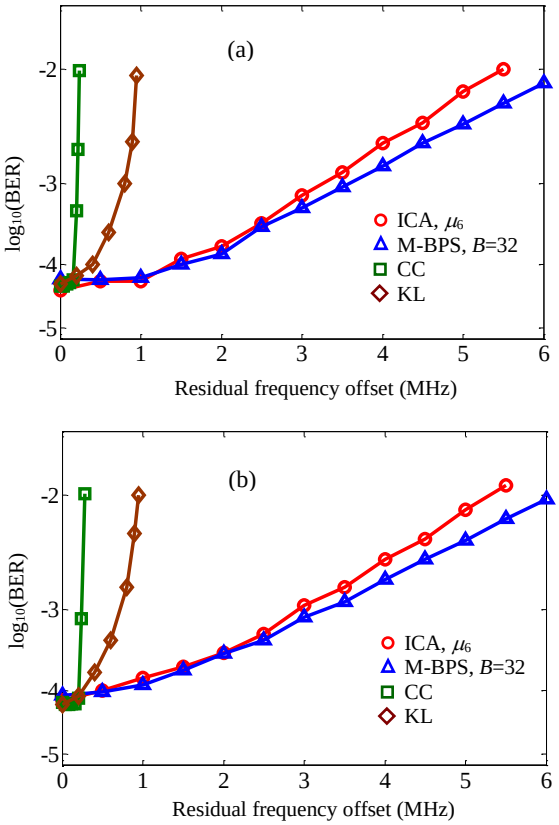

Fig. 22. Performance versus RFO at (a) 600 km and (b) 1200 km. The OSNRs in both figures are ~16 dB.

V. Conclusions

In conclusion, we propose a novel ICA-based phase compensation method for OQAM multicarrier systems, by exploiting the statistical difference between the signal and the IMI for the first time. We theoretically prove that the signal exhibits the minimal entropy with the PDF deviating from the Gaussian one the most when the phase is correctly compensated, while approaching a Gaussian distribution as the phase error

increases. We propose several metrics and a recursive algorithm for the ICA method to separate the signal and the IMI. Both simulations and experiments are performed to verify the proposed theory. It is shown that the proposed ICA method exhibits significantly better performance compared to the CC and KL methods and greatly reduces the complexity compared to the M-BPS method. This makes the ICA method the most promising solution for phase and RFO compensation in OQAM multicarrier systems.

APPENDIX I:

We will prove that the entropy of $b_{i,m}^{real}$ in Eq. (5) is minimized when the phase is correctly compensated. We consider the joint probability of Re{ $I_{i,m}^{real}$ } and Im{ $I_{i,m}^{real}$ }. It is clear that this joint probability does not change with φ_i. Therefore, the entropy H(Re{ $I_{i,m}^{real}$ }, Im{ $I_{i,m}^{real}$ }) is the same regardless of φ_i. It is also noted that when φ_i is zero, $a_{i,m}^{real}$ and $c_{i,m}^{real}$ are independent. Therefore, we have:

$$\begin{aligned} H(\mathrm{Re}\{I_{i,m}^{real}\},\mathrm{Im}\{I_{i,m}^{real}\}) &= H(a_{i,m}^{real}) + H(c_{i,m}^{real}) \\ &= H(\mathrm{Re}\{I_{i,m}^{real}\}) + H(\mathrm{Im}\{I_{i,m}^{real}\}) - I(\mathrm{Re}\{I_{i,m}^{real}\},\mathrm{Im}\{I_{i,m}^{real}\}) \end{aligned} \quad (8)$$

where I(Re{ $I_{i,m}^{real}$ }, Im{ $I_{i,m}^{real}$ }) is the mutual information of Re{ $I_{i,m}^{real}$ } and Im{ $I_{i,m}^{real}$ } and is no less than zero. On the other hand, because the variances of $a_{i,m}^{real}$ and $c_{i,m}^{real}$ are σ^2, from Eq. (4), it is readily calculated that the variances of Re{ $I_{i,m}^{real}$ } and Im{ $I_{i,m}^{real}$ } are also σ^2. Given the fixed variance, it is well known that the Gaussian distribution gives the maximal entropy. Because $c_{i,m}^{real}$ is Gaussian distributed, H($c_{i,m}^{real}$)≥H(Im{ $I_{i,m}^{real}$ }). On the other hand, I(Re{ $I_{i,m}^{real}$ }, Im{ $I_{i,m}^{real}$ })≥0. Therefore, we can get H($a_{i,m}^{real}$)≤H(Re{ $I_{i,m}^{real}$ }) for any φ_i. In order to enable $b_{i,m}^{real}$ = $a_{i,m}^{real}$, H($b_{i,m}^{real}$) is minimized or the PDF of $b_{i,m}^{real}$ deviates from the Gaussian distribution the most.

REFERENCES

[1] J. Zhao and A.D. Ellis, "Offset-QAM based coherent WDM for spectral efficiency enhancement," *Opt. Express*, vol. 19, pp. 14617-14631, 2011.

[2] J. Zhao, "DFT-based offset-QAM OFDM for optical communication," *Opt. Express*, vol. 22, pp. 1114-1126, 2014.

[3] Z. Li, T. Jiang, H. Li, X. Zhang, C. Li, C. Li, R. Hu, M. Luo, X. Zhang, X. Xiao, Q. Yang, and S. Yu, "Experimental demonstration of 110-Gb/s unsynchronized band-multiplexed superchannel coherent optical OFDM/OQAM system," *Opt. Express*, vol. 21, pp. 21924–21931, 2013.

[4] M. Xu, J. Zhang, F. Lu, J. Wang, L. Cheng, M.I. Khalil, D. Guidotti, and G.K. Chang, "Orthogonal multiband CAP modulation based on offset-QAM and advanced filter design in spectral efficient MMW RoF systems," *IEEE J. Lightwave Technol.*, vol. 35, pp. 997-1005, 2017.

[5] A. Saljoghei, F.A. Gutierrez, P. Perry, D. Venkitesh, R.D. Koipillai, and L.P. Barry, "Experimental comparison of FBMC and OFDM for multiple access uplink PON," *IEEE/OSA J. Lightwave Technol.*, vol. 35, pp. 1595-1604, 2017.

[6] S-Y. Jung, S-M. Jung, and S-K. Han, "AMO-FBMC for asynchronous heterogeneous signal integrated optical transmission," *IEEE Photon. Tech. Lett.*, vol. 27, pp. 133-136, 2015.

[7] J. Zhao and C.K. Chan, "Adaptively loaded SP-offset-QAM OFDM for IM/DD communication systems," *Opt. Express*, vol. 25, pp. 21603-21618, 2017.

[8] J. Zhao, "Channel estimation in DFT-based offset-QAM OFDM systems," *Opt. Express*, vol. 22, pp. 25651-25662, 2014.

[9] N-Q Nhan, P. Morel, S. Azou, M. Morvan, P. Gravey, and E. Pincemin, "Sparse preamble design for polarization division multiplexed CO-OFDM/OQAM channel estimation," *IEEE/OSA J. Lightw. Technol.*, vol. 36, pp. 2737-2745, 2018.

[10] T.H Nguyen, F. Rottenberg, S.P Gorza, J. Louveaux, and F. Horlin, "Efficient chromatic dispersion compensation and carrier phase tracking for optical fiber FBMC/OQAM systems," *IEEE/OSA J. Lightw. Technol.*, vol. 35, pp. 2909-2916, 2017.

[11] X. Fang, Y. Xu, Z. Chen, and F. Zhang, "Time-domain least square channel estimation for polarization-division multiplexed CO-OFDM/OQAM systems," *IEEE/OSA J. Lightw. Technol.*, vol. 34, pp. 891-900, 2016.

[12] F. Rottenberg, T.H. Nguyen, S.P. Gorza, F. Horlin, and J. Louveaux, "Advanced chromatic dispersion compensation in optical fiber FBMC-OQAM systems," *IEEE Photon. J.*, vol. 9, 2017.

[13] Z. Zheng, F. Frey, P.W. Berenguer, and J.K. Fischer, "Low-complexity equalization scheme for multicarrier offset-QAM systems," *IEEE Photon. Technol. Lett.*, vol. 29, pp. 2075-2078, 2017.

[14] J. Zhao and P. Townsend, "Fast channel estimation and equalization scheme for offset-QAM OFDM systems," *Opt. Express*, vol. 27, pp. 714-728, 2019.

[15] D. Wang, L. Yuan, J. Lei, G. Wu, S. Li, R. Ding, and D. Wang, "Joint channel/frequency offset estimation and correction for coherent optical FBMC/OQAM system," *Opt. Fiber Technol.*, vol. 39, pp. 87-94, 2017.

[16] H. Tang, M. Xiang, S. Fu, M. Tang, P. Shum and D. Liu, "Feed-forward carrier phase recovery for offset-QAM Nyquist WDM transmission," *Opt. Express*, vol. 23, pp. 6215-6227, 2015.

[17] H. Tang, S. Fu, H. Liu, M. Tang, P. Shum, and D. Liu, "Low-complexity carrier phase recovery based on constellation classification for M-ary offset-QAM signal," *IEEE J. Lightwave Technol.*, vol. 34, pp. 1133-1140, 2016.

[18] T.H. Nguyen and C. Peucheret, "Kalman filtering for carrier phase recovery in optical offset-QAM Nyquist WDM systems," *IEEE Photon. Technol. Lett.*, vol. 29, pp. 1019-1022, 2017.

[19] A. Hyvarinen, "Survey on independent component analysis," *Neural Computing Surveys*, vol. 2, pp. 94-128, 1999.

[20] H. Zhang, Z. Tao, L. Liu, S. Oda, T. Hoshida, J.C. Rasmussen, "Polarization demultiplexing based on independent component analysis in optical coherent receivers," *European Conference on Optical Communications*, 2008, paper Mo.3.D.5.

[21] X. Li, W. Zhong, A. Alphones, C. Yu, and Z. Xu, "Channel equalization in optical OFDM systems using independent component analysis," *IEEE J. Lightwave Technol.*, vol. 32, pp. 3206-3214, 2014.